# Low-cycle fatigue behavior and deformation mechanisms of a dual-phase $Al_{0.5}CoCrFeMnNi$ high-entropy alloy

Kaiju Lu[1*], Fabian Knöpfle[1], Ankur Chauhan[1,2], H.T. Jeong[3], Dimitri Litvinov[1], Mario Walter[1], W.J. Kim[3], and Jarir Aktaa[1]

Email: *kaiju.lu@kit.edu; kaiju.lu@hotmail.com

[1] Institute for Applied Materials, Karlsruhe Institute of Technology (KIT), Hermann-von-Helmholtz-Platz 1, 76344 Eggenstein-Leopoldshafen, Germany

[2] Department of Materials Engineering, Indian Institute of Science, Bengaluru, 560012 Karnataka, India

[3] Department of Materials Science and Engineering, Hongik University, Mapo-gu, Sangsu-dong 72-1, Seoul 121-791, Republic of Korea

**Abstract**

We uncover the low-cycle fatigue response and deformation mechanisms of a dual-phase $Al_{0.5}CoCrFeMnNi$ high-entropy alloy (HEA) by comparing to CoCrFeMnNi HEA. $Al_{0.5}CoCrFeMnNi$ demonstrates higher cyclic stress resistance, meanwhile maintaining comparable cyclic strain resistance at low-to-medium strain amplitudes. Microstructural investigations revealed dislocation slip as the primary deformation mechanism, which changes from planar slip to wavy slip with increasing strain amplitude. The enhanced cyclic stress resistance is related to precipitation hardening and improved solid solution strengthening. Meanwhile, the comparable cyclic strain resistance is ascribed to their similar deformation mode. Lastly, comparison with $Al_{0.5}CoCrFeNi$ and CoCrNi alloys provide strategies for tailoring HEAs with enhanced fatigue resistance.

**Keywords:** High-entropy alloy; Dual-phase; Fatigue; Transmission electron microscopy; Dislocation.

## 1. Introduction

High-entropy alloys (HEAs) and their subsets (*i.e.*, medium-entropy alloys, MEAs) have drawn tremendous scientific interest [1-8]. Among them, those with single-phase face-centered cubic (FCC) crystal structure, such as equiatomic CoCrFeMnNi and CoCrNi alloys, have been extensively investigated due to their promising mechanical properties including excellent ductility and fracture toughness [1, 9, 10]. However, their strength is often insufficient for engineering applications at room temperature [1, 5, 6, 10]. Consequently, a strategy based on secondary phase (or precipitates) hardening, such as by minor Al addition into FCC HEAs/MEAs (*e.g.*, $Al_{0.5}$CoCrFeMnNi), has been explored and proved to effectively enhance strength without losing much of the ductility [11-15].

Apart from these extensive studies focusing on monotonic mechanical properties for dual-phase (*e.g.*, FCC matrix and body-centered cubic (BCC) precipitates) HEAs, others [16-21] have also shed light on their fatigue properties, which are critical for their potential safety-related structural applications. For example, a duplex microstructure in $AlCoCrFeNi_{2.1}$ HEA (*i.e.*, with hard BCC phase and soft FCC phase in lamellar morphology) was found to delay fatigue crack initiation [17]. Additionally, Liu et al. [19] reported on the $Al_{0.3}$CoCrFeNi HEA (with FCC matrix and hard B2 and sigma phases), which exhibits excellent fatigue resistance due to the formation of deformation twins and matrix's large dislocation accumulation capability. Furthermore, Zou et al. [15] showed that the Al addition into CoCrFeMnNi thin foils (with FCC matrix and BCC phases) effectively decreases the cyclic strain localization and improves the bending fatigue resistance. It should be noted that most of the previous studies [16-19] concentrated on the high-cycle fatigue (HCF) behavior of multiple/dual-phase HEAs, which is suggested to be better than FCC HEAs [21]. The better HCF resistance of dual-phase HEAs is as-expected, as it is generally determined more by their higher strength [22, 23].

Similar to these HCF studies, it is also vital to understand dual-phase HEAs' low-cycle fatigue (LCF) behavior. In contrast to the several recent efforts made for understanding the LCF behavior of single-phase HEAs/MEAs [24-32], investigations on the dual-phase HEAs (especially with FCC matrix and BCC intermetallic phases) and further

comparisons to FCC HEAs/MEAs are limited [20]. Such a comparison would also help identify potential features contributing to HEAs' unique fatigue properties; hence, tune them more efficiently.

To date, the LCF response of dual-phase $Fe_{50}Mn_{30}Co_{10}Cr_{10}$ HEAs (with FCC and $\varepsilon$-hexagonal closed packed phase) and deformation mechanisms have been reported [33, 34]. Recently, the only LCF study [20] on an $Al_{0.5}$CoCrFeNi dual-phase HEA (with FCC-B2 structure) unveiled that in comparison to conventional HEAs (*e.g.*, a coarse-grained FCC CoCrFeMnNi) [20], fine-grained $Al_{0.5}$CoCrFeNi exhibits higher (or comparable) LCF properties at low (or high) plastic strain amplitudes. Despite this dedicated effort, the grain size effect on the comparison in the LCF properties of dual-phase HEAs and FCC HEAs should not be neglected. For instance, for CoCrFeMnNi, reducing grain size led to longer fatigue life [25, 30].

Consequently, this work is designed to identify the LCF behavior of a fine-grained $Al_{0.5}$CoCrFeMnNi dual-phase HEA, and to further uncover the origins of the peculiarity of dual-phase HEAs (by comparing to fine-grained CoCrFeMnNi model HEA). Furthermore, by comparing it to another $Al_{0.5}$CoCrFeNi dual-phase HEA and a CoCrNi FCC MEA, this work also discusses potential strategies to tailor HEAs with enhanced fatigue resistance.

## 2. Methods

The investigated $Al_{0.5}$CoCrFeMnNi alloy was synthesized from pure metals with a nominal atomic composition (with purity > 99.99 wt.%) by vacuum arc melting. The alloy melt was cast in a quadrangle-shaped cold copper crucible. Then the as-cast ingots were homogenized at 1373 K for 6 h furnace-cooled in the Argon atmosphere. Thereafter, the homogenized ingot was subjected to hot rolling at 693 K to a thickness reduction of 50% (from 20 mm to 10 mm). Finally, the LCF cylinder specimens (with gauge length and diameter of 7.6 mm and 2 mm, respectively) were machined out from the hot-rolled plates along the rolling direction. Before tests, the specimens were annealed at 1373 K for 20 mins to obtain a recrystallized microstructure with fine-grained FCC matrix and a small amount of embedded BCC phase.

The strain-controlled LCF tests were performed at room temperature on an MTS servo-hydraulic testing machine equipped with an extensometer (gauge length: 7 mm). The fatigue tests were carried out under total strain amplitudes ($\Delta\varepsilon_t/2$) of 0.3%, 0.5%, and 0.7%. These strain amplitudes were chosen to ensure fatigue lifetime lies within the LCF regime. The symmetrical triangular waveform (strain ratio $R$=−1) was applied at a nominal strain rate of $3\times10^{-3}$ $s^{-1}$. For the same testing condition, the experiments were repeated twice to ensure the reliability of the data. The lifetime ($N_f$) was defined by using the ASTM Standard E2714-13 [35]. Additionally, the inelastic strain amplitude ($\Delta\varepsilon_{in}/2$) and stress amplitude ($\Delta\sigma/2$) at each cycle were determined from the hysteresis loop.

To reveal the microstructural evolution, as-recrystallized and/or post-fatigued microstructures were characterized using scanning electron microscopy (SEM), energy dispersive spectroscopy (EDS), electron backscatter diffraction (EBSD) and transmission electron microscopy (TEM).

A Zeiss SEM equipped with EDS and EBSD detectors was employed for SEM investigations at an accelerating voltage of 20 kV. The step size of ~ 100 nm was employed for EBSD scanning. For preparing EBSD samples, thin foils were extracted out from the gauge section of the tested specimens along the loading direction. These foils were then mechanically ground and polished, followed by vibratory polishing. The acquired EBSD data were analyzed using OIM analysis software.

To prepare TEM samples, the acquired EBSD foils were further mechanically ground to a thickness of ~ 100 μm. Thereafter, 3 mm diameter discs were punched out from the foils and finally thinned by twin-jet electro-polishing at ~ (−10) °C, and a voltage of ~ 13 V. The electrolyte consisted of perchloric acid, glycerin, and methanol with a volume fraction of 1:2:7. TEM investigations were performed on an FEI Tecnai F20 microscope operating at 200 kV.

## 3. Results

### 3.1 Initial microstructure

Fig. 1a-c display representative BSE micrograph, grain orientation map and phase map of the as-recrystallized $Al_{0.5}CoCrFeMnNi$ alloy. Evidently, the $Al_{0.5}CoCrFeMnNi$ manifests FCC matrix and BCC precipitates (with area fraction of ~ 12.5%), see Fig. 1a, c. The FCC phase exhibits an average grain size of ~ 5 μm (Fig. 1b), annealing twins (Σ3 boundaries fraction of ~ 20% [12]) and no obvious texture. The BCC precipitates exhibit two different morphologies, including fine BCC-phase embedded in the FCC grain and coarse BCC-phase located along the FCC grain boundaries (Fig. 1a-c).

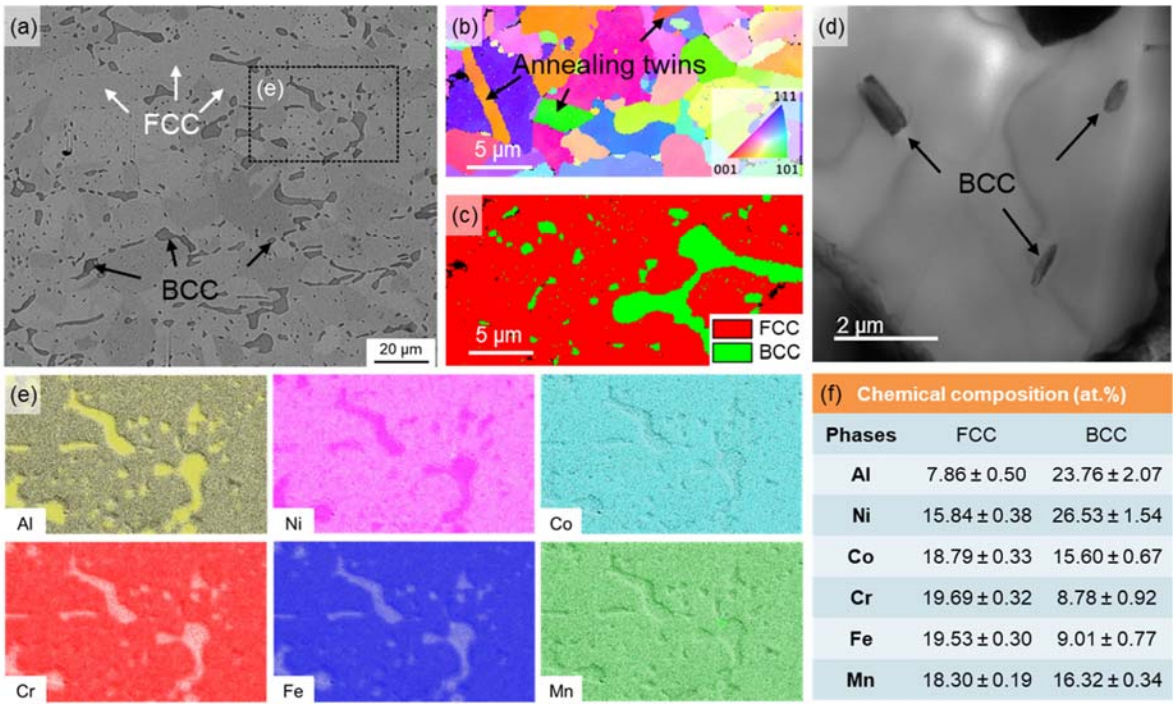


(f) Chemical composition (at.%)

| Phases | FCC | BCC |
|---|---|---|
| Al | 7.86 ± 0.50 | 23.76 ± 2.07 |
| Ni | 15.84 ± 0.38 | 26.53 ± 1.54 |
| Co | 18.79 ± 0.33 | 15.60 ± 0.67 |
| Cr | 19.69 ± 0.32 | 8.78 ± 0.92 |
| Fe | 19.53 ± 0.30 | 9.01 ± 0.77 |
| Mn | 18.30 ± 0.19 | 16.32 ± 0.34 |

Fig. 1. Microstructures of the recrystallized $Al_{0.5}CoCrFeMnNi$: (a) SEM backscattered electron (BSE) micrograph, (b) grain orientation map, (c) phase map, (d) bright-field TEM micrograph, and (e-f) EDS mapping as well as the chemical composition of the FCC and BCC phases.

Furthermore, a typical bright-field TEM micrograph shows low initial dislocation density in FCC matrix, confirming the recrystallized microstructure (Fig. 1d). Fig. 1e-f provide the chemical composition of each phase. As evident, the BCC phase is comparatively more

enriched in Ni and Al, suggesting a NiAl-type phase. Besides, via X-ray diffraction technique, the lattice parameter for FCC phase is determined to be 3.611 Å and for BCC phase to be 2.892 Å, which are consistent with Ref. [12].

### 3.2 Cyclic stress response

Fig. 2a and b show the tensile peak stress and inelastic strain amplitude *versus* the normalized number of cycles ($N/N_f$) curves for $Al_{0.5}$CoCrFeMnNi, respectively. For comparison, the LCF data of CoCrFeMnNi HEA (of fine grain size ~ 7 μm) tested at similar conditions [27] is also included. In general, similar to that of CoCrFeMnNi, the cyclic stress response of $Al_{0.5}$CoCrFeMnNi manifests three distinct stages: a sharp increase (*i.e.*, cyclic hardening stage during the first 20 to 30 cycles), followed by a noticeable decrease (*i.e.*, cyclic softening stage for about ~ 10% to 20% of the lifetime), and a gradual insignificant decrease (*i.e.*, prolonged near-steady state) until failure (Fig. 2a). This indicates that despite initial hardening and softening, most of the $Al_{0.5}$CoCrFeMnNi's LCF life is spent in a near-steady state.

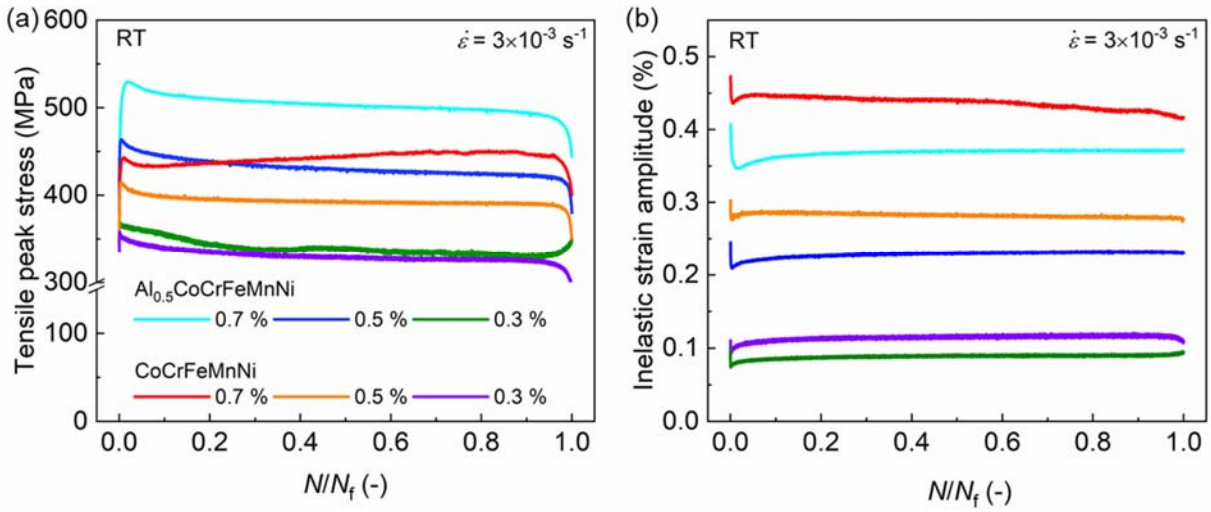


Fig. 2. (a) Tensile peak stress *versus* the *normalized* number of cycles ($N/N_f$), and (b) inelastic strain amplitude *versus* the normalized number of cycles ($N/N_f$), curves tested at different strain amplitudes, for $Al_{0.5}$CoCrFeMnNi and CoCrFeMnNi [27]. The color legends in (a) are also valid for (b).

The inelastic strain response in Fig. 2b is consistent with the evolution of the peak stresses. For instance, it shows an initial abrupt decrease followed by a gradual increase and a near-steady state until failure. Similar curves showing these evolutions (*i.e.*, tensile peak stress, inelastic strain amplitude and compression peak stress, all as a function of the number of cycles, *N*) can be found in the supplementary material (Fig. A1 and Fig. A2).

Upon comparison with the CoCrFeMnNi, $Al_{0.5}$CoCrFeMnNi shows higher cyclic strength and lower inelastic strain at all investigated strain amplitudes (Fig. 2a-b). The lower inelastic strain amplitude in $Al_{0.5}$CoCrFeMnNi is related to its higher elastic strain ($\varepsilon_e$, see Fig. 3a) due to its higher cyclic/yield strength and lower elastic modulus (or shear modulus, *i.e.*, 65.9 GPa for $Al_{0.5}$CoCrFeMnNi [36] *versus* 81 GPa for CoCrFeMnNi [37]). The higher cyclic strength and elastic strain can also be supported by their stress-strain curves at the first and half-life cycles (Fig. 3a).

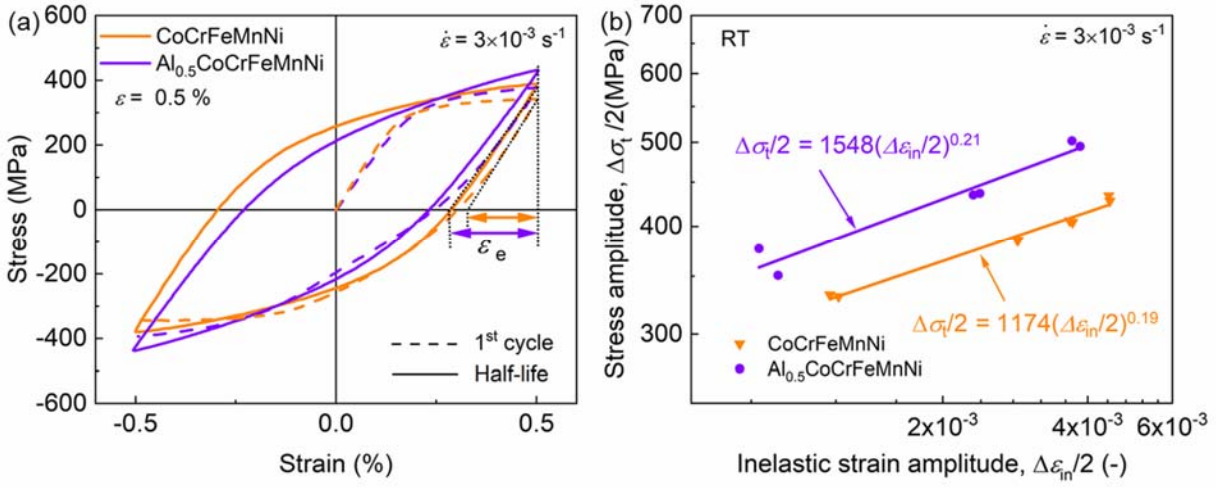


Fig. 3. (a) Stress-strain curves of the first and half-life cycles at 0.5% strain amplitude, and (b) stress amplitude *versus* inelastic strain amplitude acquired from half-life hysteresis loops, for $Al_{0.5}$CoCrFeMnNi and CoCrFeMnNi [27].

To reflect cyclic stress-strain relationship, the saturated stress amplitude and inelastic strain amplitude, acquired from half-life cycles at different strain amplitudes, were plotted in Fig. 3b for both $Al_{0.5}$CoCrFeMnNi and CoCrFeMnNi. This relationship can be approximated by a power-law equation ($\Delta\sigma/2 = K'(\Delta\varepsilon_{\mathrm{in}}/2)^{n'}$ [38], $K'$ and $n'$ are the

cyclic strength coefficient and work hardening exponent, respectively). The fitted curves and parameters ($K'$ and $n'$) are also noted in Fig. 3b.

Evidently, $Al_{0.5}$CoCrFeMnNi shows higher cyclic strength than CoCrFeMnNi for a given strain amplitude. Besides, the slope of the curve (*i.e.*, $n'$ value) of $Al_{0.5}$CoCrFeMnNi (0.21) is comparable to that of CoCrFeMnNi (0.19), suggesting their similar cyclic hardening ability with respect to the strain amplitude. A previous study indicated that the $n'$ value of FCC alloys deforming with a planar-slip mode is about one-half to two-thirds of those deforming with a wavy-slip mode [39]. Accordingly, the comparable $n'$ values of $Al_{0.5}$CoCrFeMnNi and CoCrFeMnNi imply that they likely deform by similar dislocations slip-mode, which is indeed observed by TEM investigations (see discussion section).

### 3.3 Fatigue life

To compare the lifetime between $Al_{0.5}$CoCrFeMnNi and CoCrFeMnNi, Fig. 4a and b present the saturated $\Delta\sigma/2$ *versus* $N_f$ curves (*i.e.*, Wöhler curves), and the saturated $\Delta\varepsilon_t/2$ (and/or $\Delta\varepsilon_{in}/2$) *versus* $2N_f$ curves, respectively. For a given saturated stress amplitude in Fig. 4a (*i.e.*, in the range of ~ 320−450 MPa), the $Al_{0.5}$CoCrFeMnNi exhibits longer lifetime than CoCrFeMnNi, indicating the former's higher cyclic stress resistance. For instance, at the saturated stress of ~ 425 MPa, the lifetime of $Al_{0.5}$CoCrFeMnNi is two to three times that of CoCrFeMnNi (compare the data points in the dashed square in Fig. 4a). Meanwhile, for a given $\Delta\varepsilon_t/2$ and $\Delta\varepsilon_{in}/2$ in Fig. 4b, the data for $Al_{0.5}$CoCrFeMnNi and CoCrFeMnNi almost lie on top of each other at low and medium strain amplitudes (0.3% and 0.5%), indicating their comparable cyclic strain resistance. Nevertheless, at high strain amplitude (0.7%), $Al_{0.5}$CoCrFeMnNi shows as-expect shorter life than CoCrFeMnNi (compare the data points in the dashed square in Fig. 4b).

In Fig. 4b, the LCF data were fitted by the well-known Manson-Coffin law ($\Delta\varepsilon_{in}/2 = \varepsilon'_f (2N_f)^c$ [40, 41], $c$ and $\varepsilon'_f$ are fatigue ductility exponent and coefficient, respectively). The fitted curves and parameters are also noted in Fig. 4b. The fitted $c$ value for $Al_{0.5}$CoCrFeMnNi, −0.35, is beyond the typical range ($-0.7 \le c \le -0.5$) observed for most metals [42], primarily due to the short life at high strain amplitude (0.7%). Since the parameter $\varepsilon'_f$ is related to the monotonic test's fracture strain [42], the fitted $\varepsilon'_f$ value for

$Al_{0.5}$CoCrFeMnNi (0.058) is as-expected lower than that of CoCrFeMnNi (0.47), due to $Al_{0.5}$CoCrFeMnNi's lower monotonic fracture strain.

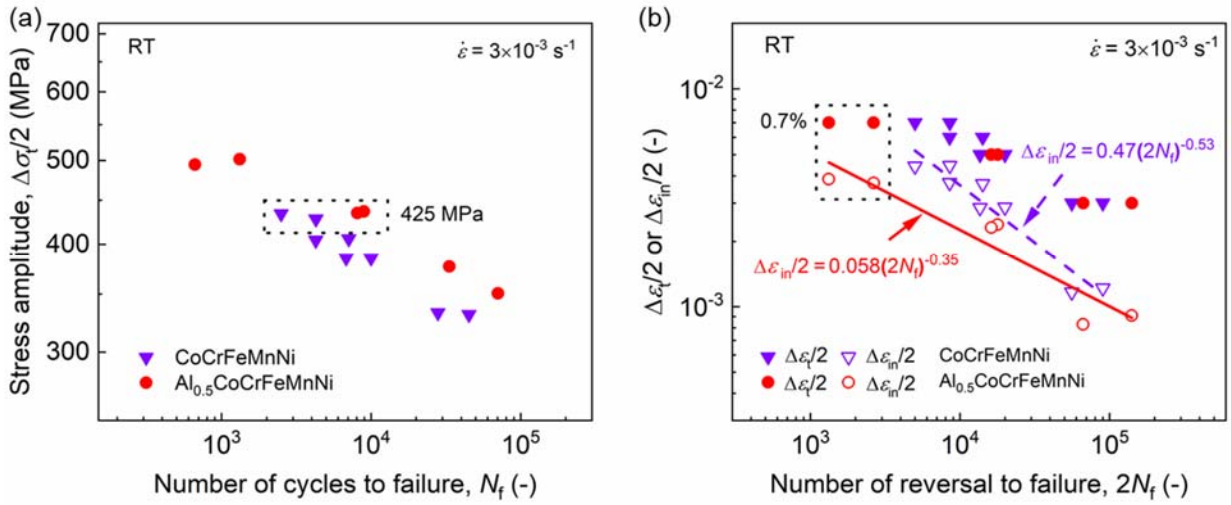


Fig. 4. Comparison of the LCF life behavior of $Al_{0.5}$CoCrFeMnNi and CoCrFeMnNi [27] [1]. Plots of (a) stress amplitude ($\Delta\sigma$/2) *versus* the number of cycles to failure ($N_f$), (b) total or inelastic strain amplitude ($\Delta\varepsilon_t$/2 or $\Delta\varepsilon_{in}$/2) *versus* the number of reversals to failure ($2N_f$).

To further explore features contributing to the peculiar LCF properties of HEAs, the data of the $Al_{0.5}$CoCrFeMnNi is compared to those of another dual-phase $Al_{0.5}$CoCrFeNi HEA [20] and FCC CoCrNi MEA [27] (see Wöhler and Manson-Coffin curves in Fig. 5a and b, respectively). By comparing to the $Al_{0.5}$CoCrFeNi alloy (*blue*), the $Al_{0.5}$CoCrFeMnNi (*red*) exhibits a shorter life at a given stress amplitude (Fig. 5a). Nevertheless, both alloys show a comparable lifetime for a given inelastic strain amplitude (Fig. 5b). Lastly, by comparing to both $Al_{0.5}$CoCrFeMnNi and $Al_{0.5}$CoCrFeNi, the CoCrNi MEA (*orange* in Fig. 5a-b) exhibits the most extended lifetime at both given stress and strain amplitude conditions, indicating its highest cyclic stress and strain resistance among these alloys.

[1] $Al_{0.5}$CoCrFeMnNi and CoCrFeMnNi samples exhibit similar fine grain size (of ~ 5−10 μm), insignificant texture, same specimen geometry and processing procedures, which ensure a relatively fair comparison.

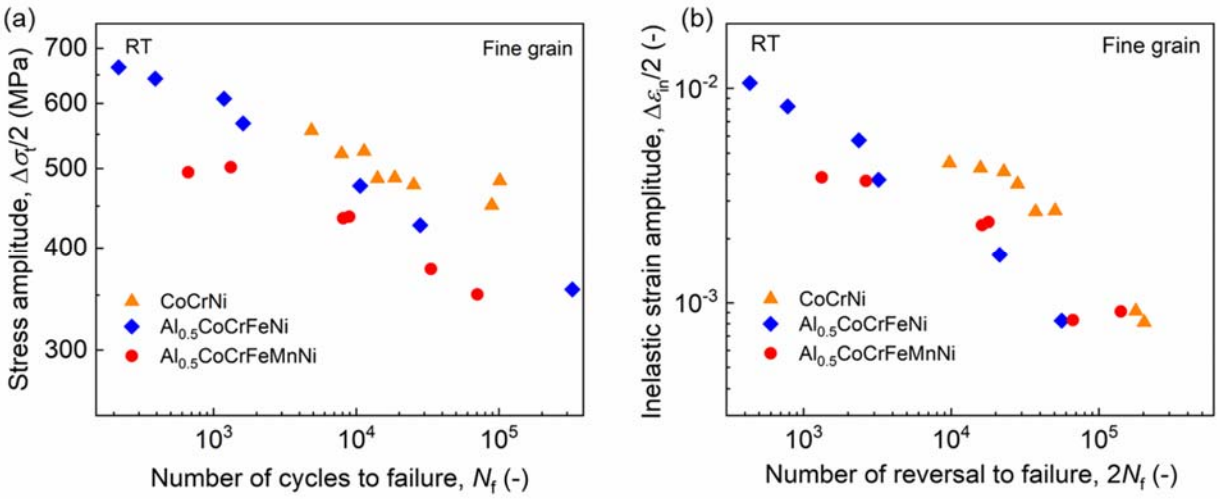


Fig. 5. Comparison of (a) Wöhler curves, and (b) Manson-Coffin curves for $Al_{0.5}CoCrFeMnNi$ and two other reference alloys ($Al_{0.5}CoCrFeNi$ [20] and CoCrNi [27]) [2].

### 3.4 Microstructure after cyclic loading

To identify operating cyclic deformation mechanisms in $Al_{0.5}CoCrFeMnNi$, the post-fractured microstructures tested at different strain amplitudes were characterized by TEM.

#### *3.4.1 Microstructure evolution upon cycling at 0.3% strain amplitude*

Fig. 6 presents representative microstructures of post-fatigued $Al_{0.5}CoCrFeMnNi$ tested at low strain amplitude of 0.3%. Evidently, the dislocation density increased compared to that in the as-recrystallized state (Fig. 1d). Furthermore, in most investigated grains, slip bands (SBs) were recognized to be the main deformation-induced features (Fig. 6a-c). Some dislocations within SBs are found to have 1/2<110> full character (not shown), while others are 1/6<112> Shockley partials (with in-between stacking faults (SFs), see the fringe contrast in the inset of Fig. 6b). Among them, full dislocations are either found to have the same or opposite Burgers vectors (*i.e.*, so-called dislocation dipoles, Fig. 6c).

[2] These materials have similar fine FCC grain sizes (of ~ 5−10 μm) and no significant texture; the $Al_{0.5}CoCrFeMnNi$ and $Al_{0.5}CoCrFeNi$ have comparable Ni-Al enriched BCC-phase fraction (~ 12%). The CoCrNi and $Al_{0.5}CoCrFeMnNi$ samples have same geometry and processing procedures. These similarities enable a relative fair comparison of their fatigue life.

The dipoles were confirmed by performing TEM tilting experiments using ***+g*/*-g*** diffraction conditions [43], *e.g.*, see Fig. A3.

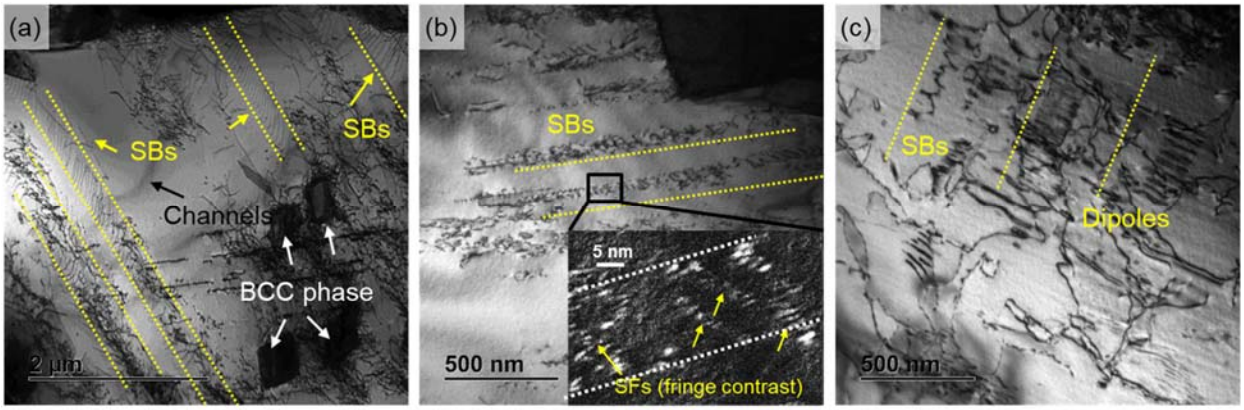


Fig. 6. TEM micrographs of post-fatigued $Al_{0.5}CoCrFeMnNi$ tested at 0.3% strain amplitude. Here, the typical microstructural features include (a) slip bands (SBs), (b) stacking faults (SFs) and (c) dipoles. (a-c) are bright-field (BF) TEM micrographs and the inset in (b) is a weak-beam dark-field TEM micrograph.

### *3.4.2 Microstructure evolution upon cycling at 0.5% and 0.7% strain amplitudes*

Fig. 7a-c and Fig. 7d-f present representative microstructures of post-fatigued $Al_{0.5}CoCrFeMnNi$ tested at medium-to-high strain amplitudes (*i.e.*, 0.5% and 0.7%, respectively). Evidently, with increasing strain amplitude from 0.3% (Fig. 6) to 0.5%/0.7% (Fig. 7), dislocation density also increases. Additionally, individual dislocations here are mostly proven to have 1/2<110> full character. In most investigated grains, the typical dislocation substructures (*i.e.*, well-defined persistent slip bands (PSB), walls, cells, and veins, separated by channels) are visible (Fig. 7a-f). Besides, dislocation dipoles are also observed sporadically (not shown here).

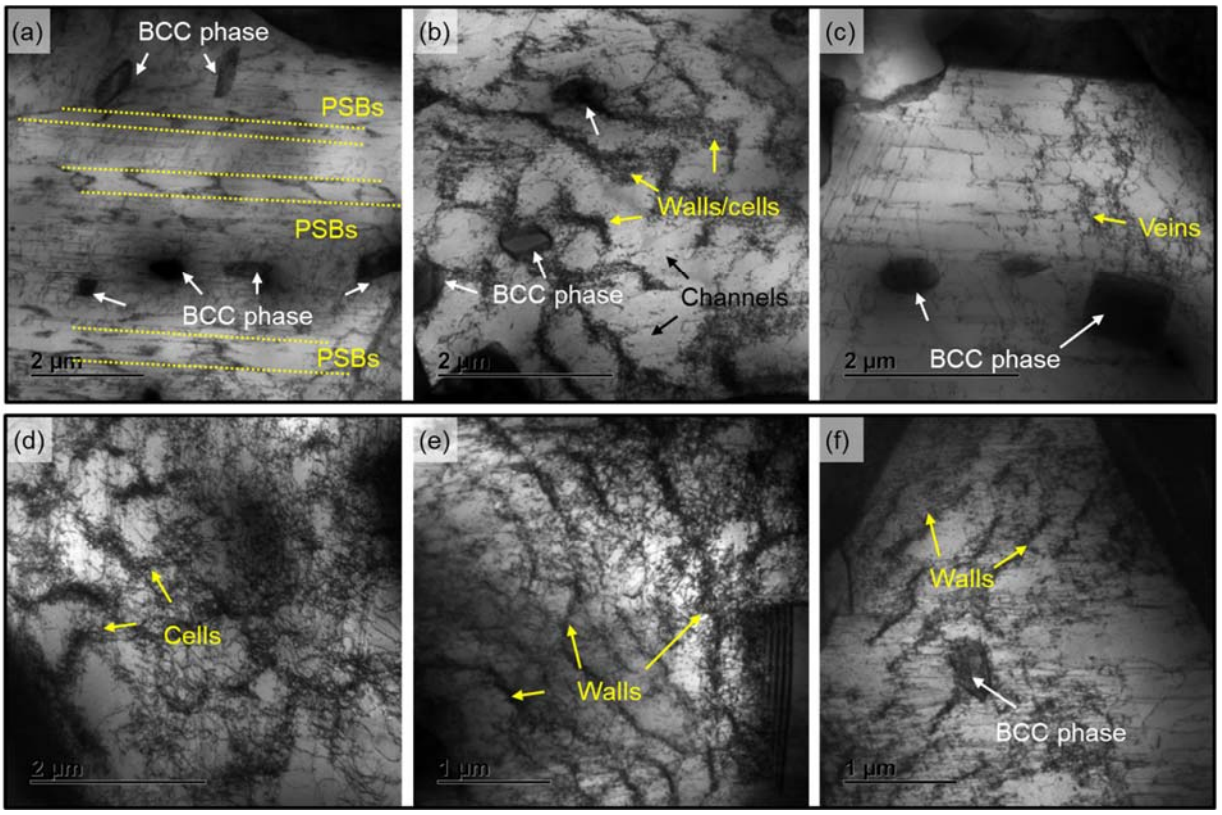


Fig. 7. TEM-BF micrographs of post-fatigued $Al_{0.5}CoCrFeMnNi$ tested at (a-c) 0.5% and (d-f) 0.7% strain amplitudes. Here, representative microstructure features include dislocation substructures, such as (a) persistent slip bands (PSBs), (b, d, e) vein/cell/wall-like substructures. (a-c, f) Extensive dislocation pileups/entanglements at FCC-BCC phase boundaries are also visible.

In addition to the above-mentioned dislocation features in the FCC matrix, extensive dislocation pileups/entanglements were observed close to the FCC-BCC phase boundaries at all investigated strain amplitudes (0.3%, 0.5% and 0.7%, see Fig. 6a and Fig. 7a-c, f). It is also worth noting that no deformation twinning could be resolved at these strain amplitudes via TEM.

## 4. Discussion

### 4.1 Deformation mechanisms

At low strain amplitude (0.3%), slip bands are recognized as the main deformation-induced features (see Fig. 6). These slip bands are also known as persistent Lüder

bands (PLBs) and typically form in planar slip materials at low strain amplitudes [44, 45]. This suggests that $Al_{0.5}$CoCrFeMnNi deforms mainly by planar slip at low strain amplitude (0.3%). The dominating planar slip herein can be ascribed to its low-to-medium stacking fault energy (SFE) and lower induced peak stresses at low strain amplitude (0.3%). The low-to-medium SFE of $Al_{0.5}$CoCrFeMnNi can be supported by the presence of annealing twins (Fig. 1b).

At medium-to-high strain amplitudes (0.5% and 0.7%), the predominantly observed dislocation substructures (*e.g.*, cells or walls separated by channels, see Fig. 7) indicate extensive wavy-slip behavior. This can be rationalized by the fact that, at medium and high strain amplitudes, higher induced peak stresses could enhance the probability of leading and trailing partials to constrict into full dislocations [25]. Specifically, the constriction of two partials into a full dislocation is aided by the so-called Escaig stress acting on the edge component of the two partials to push them together, which enhances the ability of the dislocations to cross slip [46]. Consequently, by extensive wavy/cross-slip, the simultaneous interaction (and annihilation) of dislocations with those of opposite sign Burgers vectors could lead to the formation of cells or walls (along with in-between channels) [25, 47, 48]. Together, it can be concluded that, with increasing strain amplitude from 0.3% to 0.5%/0.7%, the prevalent slip-mode changes from planar-slip to wavy-slip.

The strain-amplitude-dependent deformation mode of $Al_{0.5}$CoCrFeMnNi is similar to that of CoCrFeMnNi [25], confirming the prediction from Fig. 3b. This deformation mode evolution is also in line with the observations made in monotonically loaded CoCrFeMnNi [6], where with increasing stress levels, the initial planar slip bands changed to dislocation cell structures, indicating massive activation of cross slip.

The similar deformation mode of the $Al_{0.5}$CoCrFeMnNi and CoCrFeMnNi might be related to two factors: the degree of short-range ordering (SRO) [49] and the SFE [25, 50], as they are considered to primarily dictate the deformation mode of FCC materials. For the effect of SRO, its presence could be indirectly linked to dislocations planar slip [49]. In this study, the extensive wavy slip (for example, in the form of cells and walls, in Fig. 7) at medium-to-high strain amplitudes (0.5% and 0.7%) indicates lower influence of

SRO (if existing). Thus, our observations do not support the significant role of SRO on the $Al_{0.5}$CoCrFeMnNi's deformation mode. Since the SRO is less likely to be present in CoCrFeMnNi [25], their comparable SFE could be responsible for their similar deformation mode. And therefore, the SFE for $Al_{0.5}$CoCrFeMnNi is anticipated to be of a similar scale as of CoCrFeMnNi (30 ± 5 mJ/m$^2$ [51]).

### 4.2 Reasons for cyclic stress response

The cyclic stress response of materials is closely associated with the observed microstructural evolution. Upon initial cycling, grain-to-grain misorientations and FCC-BCC lattice misfits lead to the nucleation of a large number of dislocations close to the grain/phase boundaries. As dislocations multiply on different slip systems and spread across grains, they interact with each other (as well as with solutes and grain/phase boundaries), resulting in the initial cyclic hardening (Fig. 2).

Upon further cycling, once dislocation density becomes sufficiently high, the screw segments start to annihilate with those of opposite sign and simultaneously rearrange into stable low-energy structures, *i.e.*, dislocation high-density regions (such as SBs, PSBs, veins, and/or cells) separated by dislocation low-density regions (*i.e.*, channels) [25, 47], see Fig. 7. Once formed, the channels' presence enhances the free path of dislocation motion upon further loading; hence, causing cyclic softening [25, 31] (Fig. 2).

Afterwards, as dislocations multiply and annihilate simultaneously, a quasi-equilibrium state is reached. Therefore, a non-significant change in the dislocation densities and their structures leads to a minor change in the peak stresses (near-steady state) until failure (Fig. 2).

Apart from the above-mentioned dislocation-dislocation and dislocation-grain/phase boundaries interactions, SRO [52] and deformation twinning could also contribute to the stress response. In this study, the role of SRO and deformation twinning in the cyclic response of $Al_{0.5}$CoCrFeMnNi is minor at all investigated strain amplitudes (0.3% to 0.7%), as they were not detected.

### 4.3 Reasons for different/comparable fatigue resistance

In this work, extensive dislocation pileups/entanglements were observed at FCC-BCC phase boundaries (see Fig. 6 and Fig. 7). This suggests that the BCC phase impedes glissile dislocations, primarily due to its different elastic properties (*e.g.*, elastic modulus) and associated lattice misfit with the FCC matrix. Such dislocation interactions nevertheless provide precipitation hardening contribution in $Al_{0.5}$CoCrFeMnNi. Thus, despite a lower shear modulus, $Al_{0.5}$CoCrFeMnNi's higher yield strength (Fig. 3a) mainly originates from precipitation strengthening and higher solid solution strengthening (due to Al addition) [12], leading to its higher cyclic stress resistance, as compared to CoCrFeMnNi HEA (Fig. 4a).

Furthermore, the dislocation pileups likely consist of geometrically necessary dislocations (GNDs). This is supported by the higher kernel average misorientation (KAM) value in and around phase/grain boundaries, as indicated by the KAM map in Fig. A4. These GNDs can accommodate incompatible plastic strain between FCC and BCC phases, providing beneficial ductility to the $Al_{0.5}$CoCrFeMnNi. On the other hand, GNDs presence indicates stress concentration, which could also lead to the development of micro-cracks along the specimen's surface connected with FCC-BCC phase boundaries. Indeed, the surface cracks were broadly observed in $Al_{0.5}$CoCrFeMnNi at all investigated strain amplitudes (Fig. A5a). This is distinct from CoCrFeMnNi, where no appreciable surface cracks were observed (Fig. A5b).

Nevertheless, compared to CoCrFeMnNi, the surface cracks didn't reduce the lifetime of $Al_{0.5}$CoCrFeMnNi at low-to-medium strain amplitudes (0.3% and 0.5%, Fig. 4b). This can be rationalized by their similar deformation mode (see Section 4.1), which is generally linked with crack initiation and propagation (*i.e.*, intrusions or extrusions by forming SBs and PSBs [53]). Therefore, their similar deformation mode most likely contributed to their comparable cyclic strain resistance at low-to-medium strain amplitudes (Fig. 4b).

However, though the two materials deform in a similar mode at high strain amplitude (i.e., by wavy slip at 0.7%), a shorter lifetime is observed for $Al_{0.5}$CoCrFeMnNi compared to CoCrFeMnNi (Fig. 4b). The shorter life of $Al_{0.5}$CoCrFeMnNi suggests that other factors

(such as cracking along FCC-BCC phase boundaries) may accelerate crack initiation and propagation at higher stress/strain levels. Nevertheless, further efforts are needed to verify the relation between the observed surface cracks and FCC-BCC phase boundaries cracking.

Furthermore, in comparison to $Al_{0.5}$CoCrFeNi HEA [20] and FCC CoCrNi MEA [27], the CoCrNi MEA shows the highest cyclic stress and strain resistance (Fig. 5). The highest cyclic stress resistance of CoCrNi (Fig. 5a) is ascribed to its more severe lattice distortion due to a larger Cr percentage. This is because the higher concentration of Cr (with larger-sized atom) has the most impact on the strength of Co-Cr-Fe-Mn-Ni systems [54, 55]. Meanwhile, the highest cyclic strain resistance of CoCrNi (Fig. 5b) can be attributed to the fact that the CoCrNi mainly deforms by planar slip [27] due to its lower SFE (22 ± 4) mJ/m$^2$ [1]. The planar slip leads to more reversible dislocations motion upon forward and reverse loading, which typically promotes relatively uniform deformation; and therefore, delays micro-cracks formation in CoCrNi [27]. Together, these comparisons hint that increasing the Cr percentage (such as the Al-alloyed Co-Cr-Ni system) and reducing the SFE of the FCC phase are effective strategies to further improve the LCF performance of dual-phase HEAs.

## 5. Conclusions

This work identifies the peculiarity of the LCF response of a dual-phase $Al_{0.5}$CoCrFeMnNi HEA and advances the understanding of cyclic deformation mechanisms of dual-phase HEAs. Key findings are summarized below:

(1) Compared to FCC CoCrFeMnNi, the dual-phase $Al_{0.5}$CoCrFeMnNi manifests higher cyclic stress resistance, meanwhile preserving comparable cyclic strain resistance at low-to-medium strain amplitudes (0.3% and 0.5%). However, $Al_{0.5}$CoCrFeMnNi exhibits shorter lifetime at high strain amplitude (0.7%).

(2) Dislocations prevalent slip-mode in $Al_{0.5}$CoCrFeMnN changes from planar-slip at low strain amplitude (0.3%) to wavy-slip at medium-to-high strain amplitudes (0.5% and 0.7%). This behavior is similar to CoCrFeMnNi, which rationalizes their comparable cyclic strain resistance at low-to-medium strain amplitudes. Meanwhile,

the enhanced cyclic stress resistance of $Al_{0.5}CoCrFeMnNi$ stems from precipitation hardening and increased solid solution strengthening.

(3) At high strain amplitudes (0.7%), the shorter fatigue life of $Al_{0.5}CoCrFeMnNi$ than CoCrFeMnNi suggests that other factors such as cracking along FCC-BCC phase boundaries may accelerate crack initiation and propagation at high-stress levels.

(4) Comparison with $Al_{0.5}CoCrFeNi$ and CoCrNi alloys provide strategies for tailoring HEAs with enhanced fatigue resistance, for example, by increasing Cr percentage and reducing SFE of the FCC matrix.

## Appendix

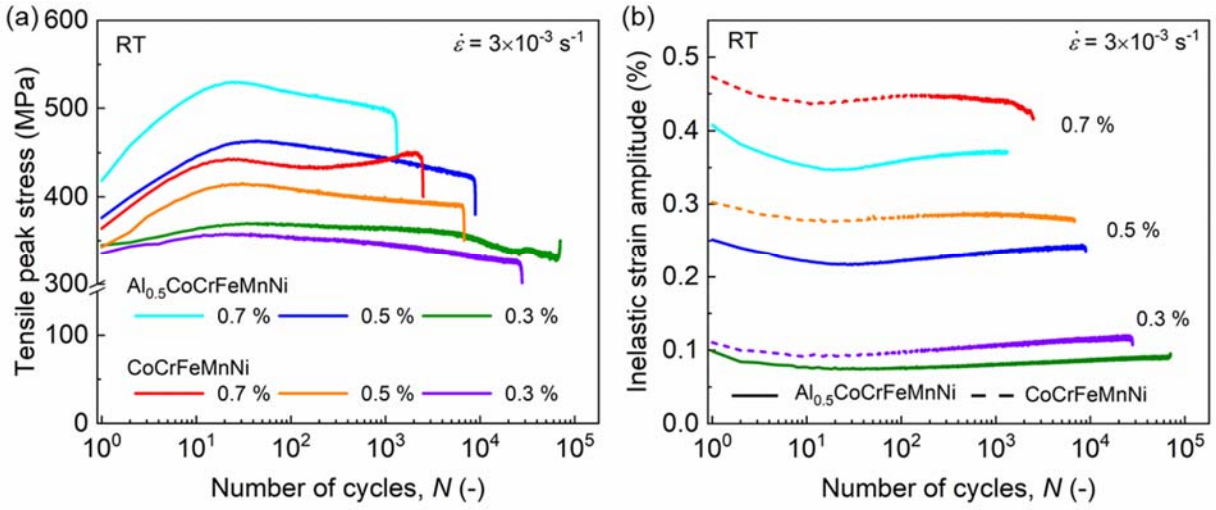


Fig. A1. (a) Tensile peak stress and (b) inelastic strain amplitude *versus* number of cycles (*N*) curves for $Al_{0.5}CoCrFeMnNi$ and CoCrFeMnNi [27] under different strain amplitudes at room temperature. Note that, in (a), for $Al_{0.5}CoCrFeMnNi$ at 0.3% strain amplitude, the peak stress increases unexpectedly near the end of the lifetime. This increase in stress originates from a primary crack that nucleated outside the probed gauge length.

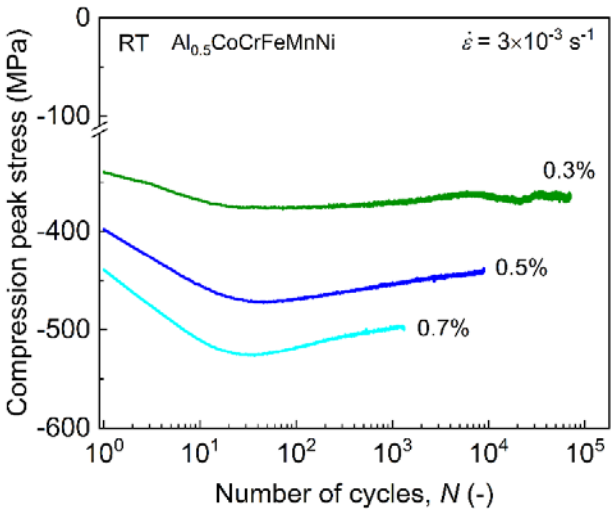


Fig. A2. Compression peak stress *versus* number of cycles (*N*) curves for $Al_{0.5}CoCrFeMnNi$ under different strain amplitudes at room temperature. The compression peak stress shows similar response as the tensile peak stress, *i.e.*, initial hardening, followed by softening and near-steady state.

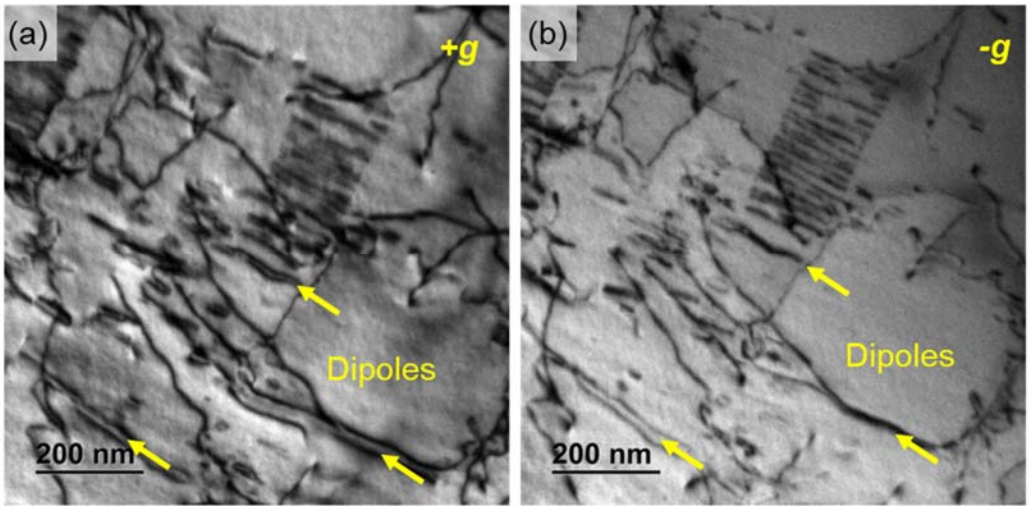


Fig. A3. (a-b) TEM micrographs from post-fatigued $Al_{0.5}CoCrFeMnNi$ tested at 0.3% strain amplitude showing dislocation dipoles. The separating distances between the dislocation pairs (arrow-indicated) change by reversing the two-beam diffraction condition (+***g***/-***g***).

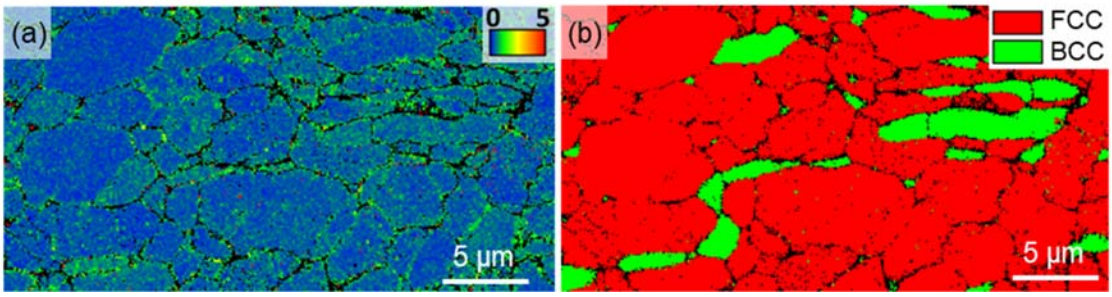


Fig. A4. (a) Kernel average misorientation (KAM) map and (b) phase map acquired from an $Al_{0.5}CoCrFeMnNi$ specimen tested at 0.5% strain amplitude. Higher KAM values close to the grain boundaries and phase boundaries indicate larger geometrical necessary dislocations density herein.

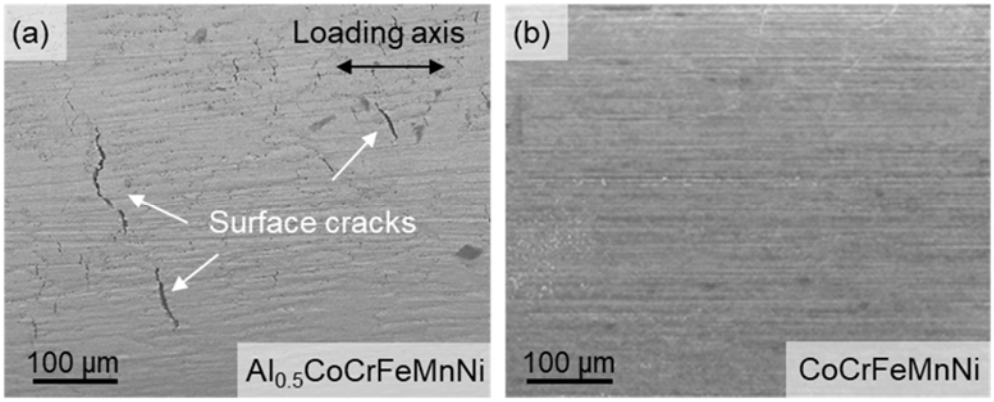


Fig. A5. SEM micrographs acquired from the surfaces of (a) $Al_{0.5}CoCrFeMnNi$ and (b) CoCrFeMnNi samples tested at 0.5% strain amplitude.

## References

[1] G. Laplanche, A. Kostka, C. Reinhart, J. Hunfeld, G. Eggeler, E.P. George, Reasons for the superior mechanical properties of medium-entropy CrCoNi compared to high-entropy CrMnFeCoNi, Acta Materialia, 128 (2017) 292-303.

[2] D. Hua, Q. Xia, W. Wang, Q. Zhou, S. Li, D. Qian, J. Shi, H. Wang, Atomistic insights into the deformation mechanism of a CoCrNi medium entropy alloy under nanoindentation, International Journal of Plasticity, 142 (2021).

[3] Q. Pan, L. Zhang, R. Feng, Q. Lu, K. An, A.C. Chuang, J.D. Poplawsky, P.K. Liaw, L. Lu, Gradient-cell-structured high-entropy alloy with exceptional strength and ductility, Science, 0 (2021) eabj8114.

[4] J. Rackwitz, Q. Yu, Y. Yang, G. Laplanche, E.P. George, A.M. Minor, R.O. Ritchie, Effects of cryogenic temperature and grain size on fatigue-crack propagation in the medium-entropy CrCoNi alloy, Acta Materialia, 200 (2020) 351-365.

[5] K. Lu, A. Chauhan, D. Litvinov, A.S. Tirunilai, J. Freudenberger, A. Kauffmann, M. Heilmaier, J. Aktaa, Micro-mechanical deformation behavior of CoCrFeMnNi high-entropy alloy, Journal of Materials Science & Technology, 100 (2022) 237-245.
[6] F. Otto, A. Dlouhý, C. Somsen, H. Bei, G. Eggeler, E.P. George, The influences of temperature and microstructure on the tensile properties of a CoCrFeMnNi high-entropy alloy, Acta Materialia, 61 (2013) 5743-5755.
[7] D.D. Zhang, J.Y. Zhang, J. Kuang, G. Liu, J. Sun, Superior strength-ductility synergy and strain hardenability of Al/Ta co-doped NiCoCr twinned medium entropy alloy for cryogenic applications, Acta Materialia, (2021) 117288.
[8] X. Feng, J. Zhang, K. Wu, X. Liang, G. Liu, J. Sun, Ultrastrong Al0.1CoCrFeNi high-entropy alloys at small scales: effects of stacking faults vs. nanotwins, Nanoscale, 10 (2018) 13329-13334.
[9] B. Gludovatz, A. Hohenwarter, K.V. Thurston, H. Bei, Z. Wu, E.P. George, R.O. Ritchie, Exceptional damage-tolerance of a medium-entropy alloy CrCoNi at cryogenic temperatures, Nat Commun, 7 (2016) 10602.
[10] G. Laplanche, A. Kostka, O. Horst, G. Eggeler, E.P. George, Microstructure evolution and critical stress for twinning in the CrMnFeCoNi high-entropy alloy, Acta Materialia, 118 (2016) 152-163.
[11] J.M. Park, J. Moon, J.W. Bae, J. Jung, S. Lee, H.S. Kim, Effect of annealing heat treatment on microstructural evolution and tensile behavior of Al0.5CoCrFeMnNi high-entropy alloy, Materials Science and Engineering: A, 728 (2018) 251-258.
[12] H.T. Jeong, W.J. Kim, Microstructure tailoring of Al0.5CoCrFeMnNi to achieve high strength and high uniform strain using severe plastic deformation and an annealing treatment, Journal of Materials Science & Technology, 71 (2021) 228-240.
[13] J.Y. He, H. Wang, H.L. Huang, X.D. Xu, M.W. Chen, Y. Wu, X.J. Liu, T.G. Nieh, K. An, Z.P. Lu, A precipitation-hardened high-entropy alloy with outstanding tensile properties, Acta Materialia, 102 (2016) 187-196.
[14] Y.L. Zhao, T. Yang, Y. Tong, J. Wang, J.H. Luan, Z.B. Jiao, D. Chen, Y. Yang, A. Hu, C.T. Liu, J.J. Kai, Heterogeneous precipitation behavior and stacking-fault-mediated deformation in a CoCrNi-based medium-entropy alloy, Acta Materialia, 138 (2017) 72-82.
[15] J.-P. Zou, X.-M. Luo, B. Zhang, Y.-W. Luo, H.-L. Chen, F. Liang, G.-P. Zhang, Enhancing bending fatigue resistance of the CoCrFeMnNi high-entropy alloy thin foils by Al addition, Materials Science and Engineering: A, 831 (2022).
[16] Z. Tang, T. Yuan, C.-W. Tsai, J.-W. Yeh, C.D. Lundin, P.K. Liaw, Fatigue behavior of a wrought Al 0.5 CoCrCuFeNi two-phase high-entropy alloy, Acta Materialia, 99 (2015) 247-258.
[17] S. Shukla, T. Wang, S. Cotton, R.S. Mishra, Hierarchical microstructure for improved fatigue properties in a eutectic high entropy alloy, Scripta Materialia, 156 (2018) 105-109.
[18] K. Liu, S.S. Nene, M. Frank, S. Sinha, R.S. Mishra, Metastability-assisted fatigue behavior in a friction stir processed dual-phase high entropy alloy, Materials Research Letters, 6 (2018) 613-619.
[19] K. Liu, M. Komarasamy, B. Gwalani, S. Shukla, R.S. Mishra, Fatigue behavior of ultrafine grained triplex Al0. 3CoCrFeNi high entropy alloy, Scripta Materialia, 158 (2019) 116-120.
[20] R. Feng, Y. Rao, C. Liu, X. Xie, D. Yu, Y. Chen, M. Ghazisaeidi, T. Ungar, H. Wang, K. An, P.K. Liaw, Enhancing fatigue life by ductile-transformable multicomponent B2 precipitates in a high-entropy alloy, Nat Commun, 12 (2021) 3588.
[21] W. Li, S. Chen, P.K. Liaw, Discovery and design of fatigue-resistant high-entropy alloys, Scripta Materialia, 187 (2020) 68-75.
[22] H. Mughrabi, H.W. Höppel, M. Kautz, Fatigue and microstructure of ultrafine-grained metals produced by severe plastic deformation, Scripta Materialia, 51 (2004) 807-812.
[23] Q. Pan, L. Lu, Improved fatigue resistance of gradient nanograined metallic materials: Suppress strain localization and damage accumulation, Scripta Materialia, 187 (2020) 301-306.

[24] M. Heczko, V. Mazánová, C.E. Slone, M. Shih, E.P. George, M. Ghazisaeidi, J. Polák, M.J. Mills, Role of deformation twinning in fatigue of CrCoNi medium-entropy alloy at room temperature, Scripta Materialia, 202 (2021).
[25] K. Lu, A. Chauhan, A.S. Tirunilai, J. Freudenberger, A. Kauffmann, M. Heilmaier, J. Aktaa, Deformation mechanisms of CoCrFeMnNi high-entropy alloy under low-cycle-fatigue loading, Acta Materialia, 215 (2021) 117089.
[26] S. Picak, T. Wegener, S.V. Sajadifar, C. Sobrero, J. Richter, H. Kim, T. Niendorf, I. Karaman, On the Low Cycle Fatigue Response of CoCrNiFeMn High Entropy Alloy with Ultra-fine Grain Structure, Acta Materialia, (2020) 116540.
[27] K. Lu, A. Chauhan, M. Walter, A.S. Tirunilai, M. Schneider, G. Laplanche, J. Freudenberger, A. Kauffmann, M. Heilmaier, J. Aktaa, Superior low-cycle fatigue properties of CoCrNi compared to CoCrFeMnNi, Scripta Materialia, 194 (2021) 113667.
[28] M.-Y. Luo, T.-N. Lam, P.-T. Wang, N.-T. Tsou, Y.-J. Chang, R. Feng, T. Kawasaki, S. Harjo, P.K. Liaw, A.-C. Yeh, S.Y. Lee, J. Jain, E.W. Huang, Grain-size-dependent microstructure effects on cyclic deformation mechanisms in CoCrFeMnNi high-entropy-alloys, Scripta Materialia, 210 (2022).
[29] S.A.A. Shams, G. Jang, J.W. Won, J.W. Bae, H. Jin, H.S. Kim, C.S. Lee, Low-cycle fatigue properties of CoCrFeMnNi high-entropy alloy compared with its conventional counterparts, Materials Science and Engineering: A, 792 (2020) 139661.
[30] A.G. Wang, X.H. An, J. Gu, X.G. Wang, L.L. Li, W.L. Li, M. Song, Q.Q. Duan, Z.F. Zhang, X.Z. Liao, Effect of grain size on fatigue cracking at twin boundaries in a CoCrFeMnNi high-entropy alloy, Journal of Materials Science & Technology, (2019).
[31] K. Lu, A. Chauhan, F. Knöpfle, J. Aktaa, Effective and back stresses evolution upon cycling a high-entropy alloy, Materials Research Letters, 10 (2022) 369-376.
[32] K. Lu, A. Chauhan, D. Litvinov, J. Aktaa, Temperature-dependent cyclic deformation behavior of CoCrFeMnNi high-entropy alloy, International Journal of Fatigue, (2022) 106863.
[33] T. Niendorf, T. Wegener, Z. Li, D. Raabe, Unexpected cyclic stress-strain response of dual-phase high-entropy alloys induced by partial reversibility of deformation, Scripta Materialia, 143 (2018) 63-67.
[34] F. Bahadur, R. Jain, K. Biswas, N.P. Gurao, Low Cycle Fatigue Behaviour of Non-equiatomic TRIP Dual-phase Fe50Mn30Co10Cr10High Entropy Alloy, International Journal of Fatigue, (2021).
[35] A. E2714-13, Standard Test Method for Creep-Fatigue Testing, ASTM International, West Conshohocken, PA, , (2013) 1-15.
[36] H.T. Jeong, H.K. Park, H.S. Kang, W.J. Kim, Operation of solute-drag creep in an AlCoCrFeMnNi high-entropy alloy and enhanced hot workability, Journal of Alloys and Compounds, 824 (2020).
[37] G. Laplanche, P. Gadaud, O. Horst, F. Otto, G. Eggeler, E.P. George, Temperature dependencies of the elastic moduli and thermal expansion coefficient of an equiatomic, single-phase CoCrFeMnNi high-entropy alloy, Journal of Alloys and Compounds, 623 (2015) 348-353.
[38] J. Morrow, Cyclic plastic strain energy and fatigue of metals, in: Internal friction, damping, and cyclic plasticity, ASTM International, 1965.
[39] C.E. Feltner, C. Laird, Cyclic stress-strain response of F.C.C. metals and alloys-I Phenomenological experiments, Acta Metallurgica, 15 (1967) 1621-1632.
[40] S.S. Manson, Behavior of materials under conditions of thermal stress, National Advisory Committee for Aeronautics, 1953.
[41] L. Coffin Jr, A study of the effects of cyclic thermal stresses on a ductile metal, Transactions of the American Society of Mechanical Engineers, New York, 76 (1954) 931-950.
[42] S. Suresh, Fatigue of materials, Cambridge university press, 1998.
[43] P. Hirsch, A. Howie, R. Nicholson, D. Pashley, M. Whelan, L. Marton, Electron microscopy, PhT, 19 (1966) 93.

[44] R. Li, Y.-D. Wang, W. Liu, C. Geng, Q. Xie, D.E. Brown, K. An, Multiscale mechanical fatigue damage of stainless steel investigated by neutron diffraction and X-ray microdiffraction, Acta Materialia, 165 (2019) 336-345.
[45] L. Buchinger, A.S. Cheng, S. Stanzl, C. Laird, The cyclic stress-Strain response and dislocation structures of Cu16 at.%Al alloy III: Single crystals fatigued at low strain amplitudes, Materials Science and Engineering, 80 (1986) 155-167.
[46] D. Hull, D.J. Bacon, Introduction to dislocations, Butterworth-Heinemann, 2001.
[47] H. Mughrabi, Dislocation wall and cell structures and long-range internal stresses in deformed metal crystals, Acta Metallurgica, 31 (1983) 1367-1379.
[48] M.S. Pham, S.R. Holdsworth, K.G.F. Janssens, E. Mazza, Cyclic deformation response of AISI 316L at room temperature: Mechanical behaviour, microstructural evolution, physically-based evolutionary constitutive modelling, International Journal of Plasticity, 47 (2013) 143-164.
[49] V. Gerold, H.P. Karnthaler, On the origin of planar slip in f.c.c. alloys, Acta Metallurgica, 37 (1989) 2177-2183.
[50] P. Li, S. Li, Z. Wang, Z. Zhang, Fundamental factors on formation mechanism of dislocation arrangements in cyclically deformed fcc single crystals, Progress in Materials Science, 56 (2011) 328-377.
[51] N.L. Okamoto, S. Fujimoto, Y. Kambara, M. Kawamura, Z.M. Chen, H. Matsunoshita, K. Tanaka, H. Inui, E.P. George, Size effect, critical resolved shear stress, stacking fault energy, and solid solution strengthening in the CrMnFeCoNi high-entropy alloy, Scientific Reports, 6 (2016) 35863.
[52] R. Zhang, S. Zhao, J. Ding, Y. Chong, T. Jia, C. Ophus, M. Asta, R.O. Ritchie, A.M. Minor, Short-range order and its impact on the CrCoNi medium-entropy alloy, Nature, 581 (2020) 283-287.
[53] J. Polák, V. Mazánová, M. Heczko, I. Kuběna, J. Man, Profiles of persistent slip markings and internal structure of underlying persistent slip bands, Fatigue & Fracture of Engineering Materials & Structures, 40 (2017) 1101-1116.
[54] N.L. Okamoto, K. Yuge, K. Tanaka, H. Inui, E.P. George, Atomic displacement in the CrMnFeCoNi high-entropy alloy – A scaling factor to predict solid solution strengthening, AIP Advances, 6 (2016) 125008.
[55] S. Yoshida, T. Bhattacharjee, Y. Bai, N. Tsuji, Friction stress and Hall-Petch relationship in CoCrNi equi-atomic medium entropy alloy processed by severe plastic deformation and subsequent annealing, Scripta Materialia, 134 (2017) 33-36.